Studies of crack dynamics in clay soil
I. Experimental methods, results, and morphological quantification

H.-J. Vogel*, H. Hoffmann, K. Roth

University of Heidelberg, Institute of Environmental Physics, INF 229, 69120 Heidelberg, Germany

Abstract

We propose a small set of fundamental geometric measures which provide a quantitative description of crack patterns at the soil surface including their dynamics. These measures (Minkowski numbers) are combined with tools of mathematical morphology to obtain Minkowski functions. Additionally, we measured the distribution of angles within the crack network to characterize the form of aggregates. The methods are demonstrated for two experiments using different mixtures of sand (S) and bentonite (B). We found that the different crack patterns can be clearly distinguished both with respect to the dynamics of crack formation and with respect to the final crack pattern. In contrast, the frequency distribution of angles within the crack pattern was found to be invariant which is supposed to reflect the common physical processes of crack formation.
© 2004 Elsevier B.V. All rights reserved.

1. Introduction

In clay soil, the porous structure changes with the water content due to the swell–shrink dynamics of the material. Consequently, the conditions for water flow and solute transport are not stationary material properties. This is a serious difficulty for modeling flow and transport in clay soil. Such models require both a dynamic description of the hydraulic properties of the bulk soil matrix and a dynamic description of the crack pattern. The latter constitutes a network of macropores which is highly significant for water infiltration into the soil as well as for evaporation.

The dynamics of bulk soil hydraulic properties in clay soil may be derived from models of pore geometry (Tuller and Or, 2003) or by coupling water flow and the deformation of soil (Kim et al., 1999). In this paper, we focus on the crack pattern which develops at the soil surface during desiccation.

The quantification of crack patterns is typically reduced to the soil surface which is easily accessible or to two-dimensional sections through impregnated

samples. Here, the crack pattern can be characterized in terms of the distribution of crack lengths and width (O'Callaghan and Loveday, 1973; Scott et al., 1986), the size distribution of aggregates (Velde, 1999), or the fractal properties of the crack pattern (Preston et al., 1997; Velde, 1999). Using concepts of stereology, three-dimensional properties of the crack pattern may also be inferred from two-dimensional observations (Hallaire, 1989; Vogel et al., 1993), provided the structure is stationary. A direct three-dimensional investigation of soil cracks was recently approached through geoelectrical measurements by Samouëlian et al. (2003).

There is a large body of possible measures that can be taken from digitized images to quantify soil structure, and many corresponding papers were published in the last two decades (e.g., Ringrose-Voase and Bullock, 1984; Moran, 1994). In this paper, a quantitative description of cracks at the soil surface is proposed, which is based on fundamental geometric properties, the $d+1$ Minkowski numbers, M_k, where d is the dimension of the structure. For the two-dimensional crack pattern at the soil surface, we get M_0, the surface area of cracks, M_1 the length, and M_2 the Euler number of the crack network. These measures are well defined, and there exist efficient algorithms for computing them. Combined with tools from mathematical morphology, they provide an almost comprehensive geometric description including size distribution and topology of the crack pattern. The dynamics of crack formation is quantified through time series of M_k. The geometric quantification using Minkowski numbers is generic and can be applied to any type of structure also in three dimensions. As an additional descriptor, especially suited for two-dimensional crack patterns, the dynamic distribution of angles within the crack network is measured which provides information on the processes of crack formation.

The power of the proposed approach to distinguish characteristic types of crack patterns including their dynamics is demonstrated for simple experiments performed with mixtures of sand (S) and bentonite (B). The measured geometric dynamics is interpreted in terms of the physical processes acting during crack formation. Quantifying the structural dynamics is a prerequisite for the eventual quantitative simulation of cracking soils.

2. Experiments

To produce crack patterns, different mixtures of sand (S) and bentonite (B), 1:1 and 5:1, in the following referred to as SB1:1 and SB5:1, respectively, were used. Sand and bentonite were mixed with water using a mixer to get a paste with optimal consistency. The mass ratio of solid to water was 0.7 and 1.6 for SB1:1 and SB5:1, respectively. The mixtures were distributed on glass plates with a size of 24×30 cm. The clay layer had a constant thickness of 5 mm. The surface was uniformly illuminated with oblique incident light from four halogen lamps, and a digital camera was installed to record the surface during desiccation at fixed time intervals of 20 min. The two experiments were carried out in succession using the same experimental setup and the same conditions for desiccation in terms of temperature and relative humidity. The final crack patterns obtained after complete desiccation are shown in Fig. 1. In this figure, only the central part of 20×20 cm is shown. This part was almost free of artefacts caused by boundary effects and was used for further analysis. The resolution of the digital images was 0.5 mm/pixel.

3. Image processing

The contrast in grey level between cracks and aggregates was sufficiently high, so that the obtained digital images could be segmented into cracks and aggregates using a simple grey threshold. However, during desiccation, the mean grey level of the clay matrix increases considerably with decreasing water content. Moreover, the grey values were locally different even in single images because of the nonuniform drying of the material as a result of the specific air circulation during the experiment. Therefore the segmentation threshold $\hat{g}_{x,i}$ was chosen for each individual image i and for each location x as a proportion of the local mean $\bar{g}_{x,i}$, which was obtained as the mean grey value within a window of 20×20 pixel centered at x. We chose $\hat{g}_{x,i} = 0.65\ \bar{g}_{x,i}$.

Another difficulty for image segmentation occurred towards the end of crack formation, especially for the material with the higher clay content, SB1:1. Some material stuck to the glass plate inside
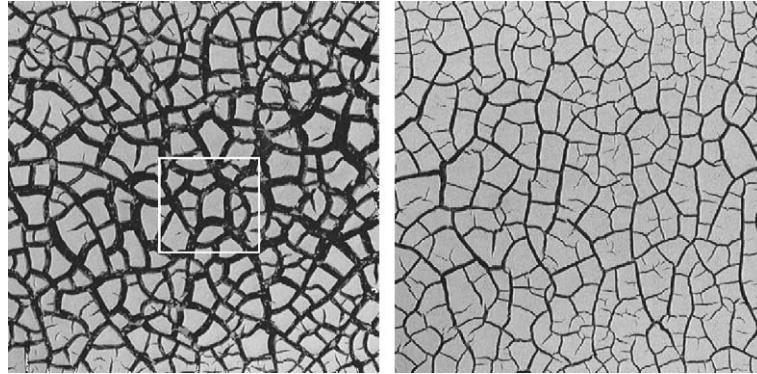
Fig. 1. Crack patterns after desiccation of mixtures of sand (S) and bentonite (B), SB1:1 (left) and SB5:1 (right), in a square frame with 20 cm side. The marked cutout of SB1:1 is used in following figures to illustrate the different analysis.

the cracks (see Fig. 1). This material has a similar grey level to the aggregates when the crack is wide enough that light can reach the glass plate directly. To avoid the related artefacts, we used again the knowledge about the type of structure and its dynamics to optimize the segmentation algorithm. For the segmentation of each image i, we use the segmented image of the earlier time step i-1. Once a crack was detected at a given point based on $\hat{g}_{x,i}$, this point is attributed to the crack network also in the following images. This simple procedure could be applied because of the fact that cracks widen during the experiment. However, the aggregates may move to some extent especially in the final stage of desiccation. Consequently, a pixel x_i that was clearly detected as a crack in image i-1 may

be at the border of an aggregate in the image i. We account for this special feature by applying the abovementioned rule only if x_i is not at the border of an aggregate. Therefore, we keep track of the boundary line of the aggregate during the segmentation procedure.

The result of the segmentation for different stages during desiccation is shown in Fig. 2 for a cutout of SB1:1. As compared to the grey scale image (Fig. 1), the artefacts are removed. Cracking starts at some locations, and single cracks propagate while growing at their tips. At some point, growing cracks branch, typically at an angle of about 120°, or a growing crack rejoins an already existing crack, typically at an angle of about 90°.
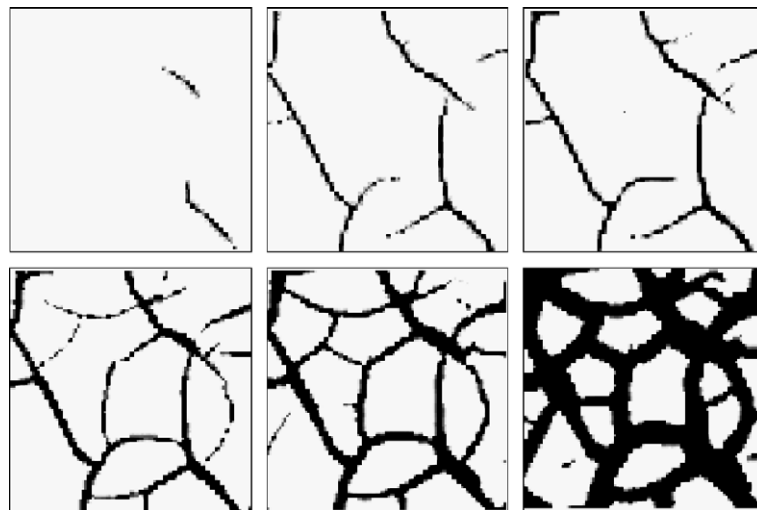

Fig. 2. Different stages of crack pattern formation during desiccation in the square cutout of SB1:1 indicated in Fig. 1.

4. Geometric measures

4.1. Minkowski numbers

To quantify the dynamics of the crack network, we start with three fundamental properties: the area A, the length L, and the topology measured by the Euler number χ of the cracks (see below). In the more general context of integral geometry, these three properties are defined for an d-dimensional structure through $d+1$ Minkowski numbers M_k with $k \in [0,\ldots,d]$. Thereby, M_0 is the total mass of the structure, in our case the area of the cracks

$$M_0(X) = A(X) \ [L^2] \qquad (1)$$

where we consider the set of black pixels X in the binary images. The other Minkowski numbers $M_{1\ldots n}$ are defined as integrals over the boundary δX of the structure X. Specifically,

$$M_1(X) = \int_{\delta X} ds = L(X) \ [L] \qquad (2)$$

where ds is the boundary element and

$$M_2(X) = \int_{\delta X} \frac{1}{r} ds = 2\pi\chi(X) \ [-] \qquad (3)$$

where r is the radius of curvature of the boundary, which is positive for convex and negative for concave boundaries. The integral in Eq. (3) measures the total curvature of the structure, which yields the value 2π for each closed convex boundary, and -2π for each closed concave boundary. Hence, as given by Eq. (3), M_2 is directly related to the Euler number χ, which is defined as the number of isolated objects N (closed convex) minus the number of holes H (closed concave), i.e., $\chi = N - H$. M_2 is a topological measure describing the connectivity of the structure with decreasing values for increasing connectivity.

To compare images of different size, we relate the Minkowski numbers to the size $\Omega \ [L^2]$ of the image to obtain Minkowski densities

$$m_k(X) = \frac{M_k}{\Omega} \ [L^{-k}] \qquad (4)$$

except for m_2, where we chose $m_2 = M_2/(2\pi\Omega)$ to get the density of the Euler number which we feel is more intuitive.

The Minkowski numbers are fundamental properties according to Hadwiger's theorem (Hadwiger, 1957), which states that all other properties of a given structure which are motion invariant, continuous, and additive can be directly calculated from these numbers. For a comprehensive discussion, see Mecke (2000). Ohser and Mücklich (2000) demonstrated that Minkowski numbers can be calculated efficiently from binary images of the structure. This approach is also possible for three-dimensional structures and was applied to the pore structure of an impregnated soil sample by Vogel et al., 2002.

Though the mean size of aggregates or the mean connectivity of the crack network can be derived from the Minkowski densities, there is no information about the size distribution of aggregates or about the numerical density of aggregates as long as they are not completely surrounded by cracks. This is because the Minkowski densities are integral measures of the entire boundary line of a given structure. Hence, a more detailed description is desirable, which can be obtained through Minkowski functions.

4.2. Minkowski functions

To get a more comprehensive characterization of the structure, the Minkowski densities can be calculated as a function of morphological transformations. This approach was proposed by Mecke (2000), who introduced the *Minkowski functions*, which are based on a transformation used in mathematical morphology, i.e., morphological erosion (Serra, 1982). The basic idea is to recalculate the Minkowski densities for a series of erosions using circular structuring elements of increasing size. An erosion of a structure X, i.e., a set of black pixels, by a circular structuring element $B_{x,r}$ with radius r and centered at the point x is defined as

$$X_e = X \ominus B_{x,r} = \{x : B_{x,r} \subset X\}. \qquad (5)$$

This means the eroded structure X_e is the set of pixels, where the structuring element is completely part of X. Hence, an erosion removes all pixels which are closer to the boundary line than r. Based on successive erosions, it is possible to attribute a grey value to each pixel that corresponds to the orthogonal distance of that pixel to the nearest crack boundary.
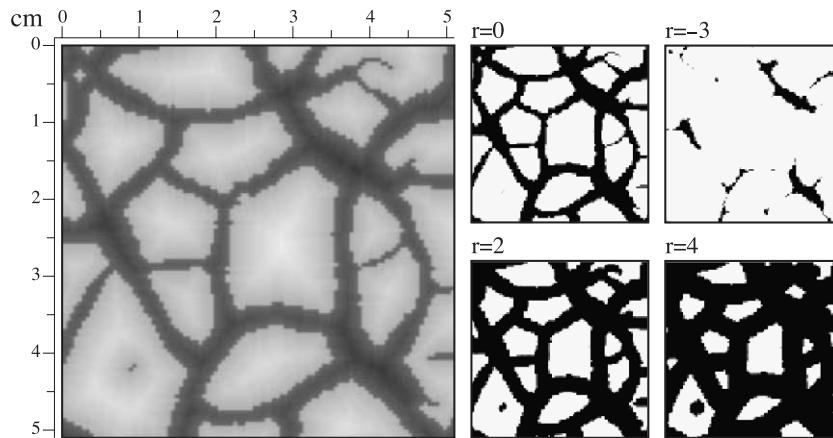
Fig. 3. The distance map (left) for the square cutout of SB1:1, and different steps r of erosions obtained by thresholding the distance map at different levels.

This can be done for pixels within soil aggregates, as well as for pixels within the cracks. The first is obtained through erosions of the aggregates, the latter through erosions of the cracks.

The resulting grey scale image will be referred to as the 'distance map' of a binary image. In Fig. 3, an example of such a distance map is shown together with different erosions. We indicate the erosion of cracks by a negative sign of r in contrast to the erosion of aggregates.

Once the distance map is calculated, the different erosions can be recovered through a segmentation of the grey image according to different thresholds. To obtain the Minkowski functions $m_0(r)$, $m_1(r)$, and $m_2(r)$, the Minkowski densities are calculated for the different erosion steps r. An example for the crack pattern in SB1:1 (Fig. 1) is given in Fig. 4. There, the values for $r=0$ correspond to the Minkowski densities of the original crack pattern.

The area density function $m_0(r)$ reflects the size distribution of the aggregates for $r>0$ and the size distribution of cracks for $r<0$. The length density function reflects both the size distribution and the connectivity of the crack pattern. For isolated cracks, the length density first increases, while for a well-connected network, it decreases with r. The Euler number $m_2(r)$ is a pure topological measure which reaches a minimum for a certain value r^*, where all potential aggregates, also those which are not completely separated by cracks at $r=0$, are separated. Hence, it yields a measure for the number of aggregates, and for $r>r^*$, it reflects approximately the size distribution of aggregates in terms of their numerical density.

The Minkowski functions thus provide a first-order description of the structure. In this way, the crack pattern can also be analyzed for different stages of crack formation to get a quantitative description of the
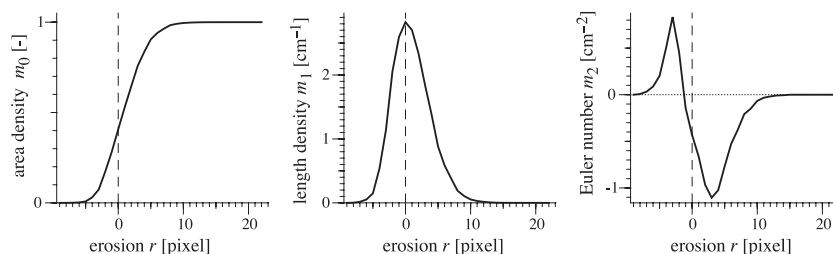

Fig. 4. Minkowski functions for the crack pattern of SB1:1. A positive sign of r is related to erosion of the aggregate, and negative sign to the erosion of the cracks, respectively. The original structure is indicated as $r=0$.

dynamics. However, the morphological shape of the aggregates or the cracks, respectively, are barely captured by the Minkowski functions. Therefore, an additional analysis of the type of branching of the crack network is added to the analysis.

4.3. Angles of bifurcation

As already discussed for the experiments, the angles of bifurcation might be a characteristic feature of a crack pattern. Moreover, as discussed further below, this feature might be related to the physical processes of crack formation. Hence, the distribution of angles was chosen as a shape descriptor.

Given the binary image of the cracks, the branching points have to be defined. This was done based on a skeleton of the cracks. To obtain the skeleton, all crack pixels that are not relevant for the topology of the structure are removed. Such pixels are identified locally by certain pixel configurations within a 3×3 window. These basic configurations are shown in Fig. 5, where the crack pixels are hatched, the matrix pixels are indicated by a circle, and pixels which are not relevant are empty. For each such configuration, including all four rotations, the central pixel was removed. This was done in an iterative process until no more redundant pixels were present. In this way, successive layers are removed, such that the skeleton forms at the center of the structure. Thereby, branching points appear with well-defined angles (Fig. 5).

Branching points are defined as pixels that have more than two direct neighbors. Thereby, only the four direct neighbors of each pixel are considered. The angle of bifurcation was measured after placing a frame of 7×7 pixels centered at the branching point, and calculating the angles between the adjacent intersection points of the frame with the skeleton as illustrated in Fig. 5. The separated intersection points are identified by scanning the frame clockwise considering the transitions from crack skeleton to background. If a branch is too short to intersect the frame, the corresponding branching point is ignored—one such example is present in the skeleton shown Fig. 5 (middle, above center). To obtain the frequency distribution of angles, the possible range between $0°$ and $180°$ was divided into 12 classes corresponding to the number of discrete angles that can be defined within a 7×7 grid. This constitutes classes having a width of $15°$ each. Due to the discrete geometry of the squared pixels, these classes are not represented with the same probability. We correct for this effect by dividing the relative frequency measured for each class by the corresponding probability of that class.

5. Results and discussion

The results of the Minkowski densies during desiccation and crack development are shown in Fig. 6 for the two experiments SB1:1 and SB5:1. Clearly,
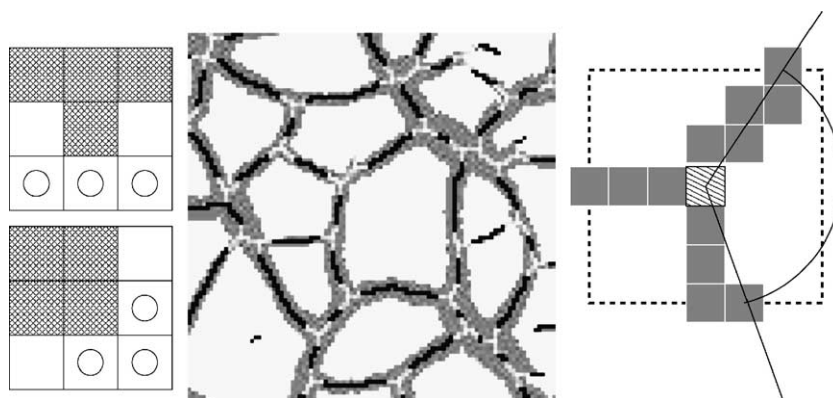

Fig. 5. Left: basic configuration of crack pixel (hatched) and matrix pixel (circles), where the central pixel is removed to generate the skeleton (see text). Middle: skeleton (black) of the crack pattern in Fig. 3 (dark grey), with bifurcation areas (light grey) and branching points (white) to calculate the angles. Right: example for the determination of the bifurcation angle in a window of 7×7 pixel centered at a branching point.
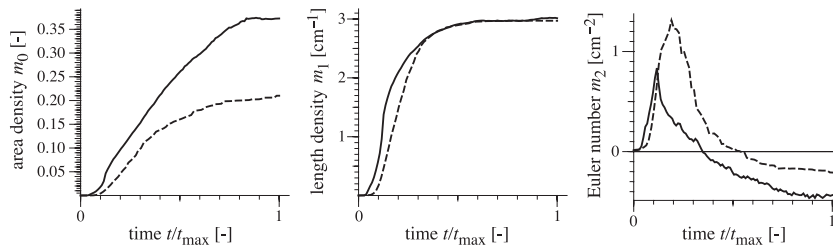
Fig. 6. Minkowski densities as a function of time during crack formation until the final crack pattern is reached at $t=t_{max}$ for the crack patterns of SB1:1 (solid line) and SB5:1 (dashed line).

the material with the lower clay content, SB5:1, shrinks less, which is obvious from the lower area density of the cracks reached at the final stage of crack formation. The type of crack dynamics is obviously different. In the clay-rich material, SB1:1, the area density increases more abruptly at the beginning of crack formation, then, after the crack network has formed, the aggregates shrink at a lower rate. The same phenomenology can be seen in the dynamics of the length densities. In contrast, crack formation in SB5:1 is characterized by a more homogeneous process, and there is no evidence for a separation in different phases of crack formation.

The evolution of the network topology shows the appearance of isolated cracks in the initial stage of crack formation as indicated by positive Euler numbers. In SB5:1, there are more isolated cracks (higher values of m_2), which become interconnected later during the desiccation process compared to SB1:1. The latter is indicated by the shift of the curves with respect to time. This reflects the early formation of the complete crack network in the clay-rich material that was also observed experimentally.

Remarkably, the length density of the final crack pattern is almost identical for the two experiments, although the area density and the connectivity of the crack network are considerably lower in SB5:1. As will be quantified through the Minkowski functions below, this is due to the more intense shrinkage of the clay-rich material SB1:1.

In Fig. 7, the Minkowski functions are shown for different stages during crack formation. The overall shape of the curves is similar for the two different materials. However, the final crack pattern is approached quicker in SB5:1 due to the lower water content, the reduced shrinkage, and possibly the faster moisture loss. This is reflected by the shape of all

three Minkowski functions, which approach their final form much quicker for SB5:1.

The continuous shrinkage of SB1:1 leads to smaller aggregates and wider cracks than that of SB5:1. This is indicated by the position of $m_0(r)$ relative to $r=0$, because the values for $r>0$ reflect the size distribution of aggregates, and those for $r<0$ the size distribution of cracks. Note that the time series of the Minkowski densities for the crack pattern itself (shown in Fig. 6) is now located on the line for $r=0$ indicated in Fig. 7. Thus, the difference in absolute crack surface is reflected by the values for $m_0(0)$.

As already discussed for the Minkowski densities, the length densities $m_1(0)$ for both crack patterns are almost identical with values of about 3 cm/cm^2. Hence, the increased width of cracks in SB1:1 is compensated by the reduced size of aggregates to end up with the same crack lengths compared to SB5:1. It might be hypothesized that for a given type of clay and a given system size in terms of surface area and thickness of the layer, this parameter comes out to be invariant for different clay contents. More experiments are needed to verify that point however.

The shape of $m_2(r)$ for $r>0$ also reflects the different size distribution of aggregates. The area enclosed by $m_2(r)$ and the line for $m_2=0$ is approximately the same for the two different materials. This indicates that the total number density of aggregates is approximately the same (which is consistent with the same length density of cracks). However, the shape of $m_2(r>0)$ reflects the broader size distribution in SB5:1. Equivalently, the curve for $m_2(r<0)$ shows the same number of cracks but a broader size distribution in SB1:1.

The results for the angles of bifurcation is shown in Fig. 8. The similarity found for the different materials is striking. There are two maxima in the frequency
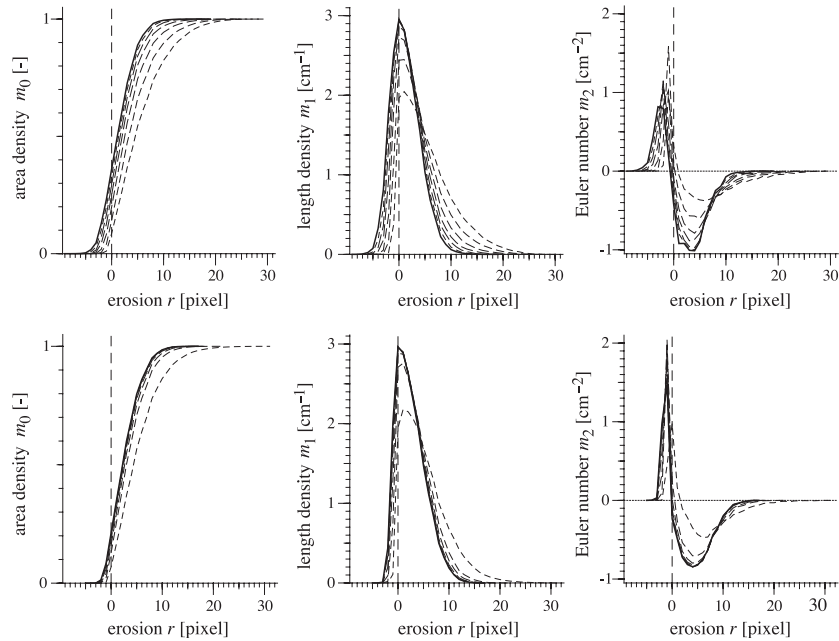
Fig. 7. Minkowski functions after seven time intervals $\Delta t = t_{max}/7$ (dash lengths increase with time) for the crack patterns of SB1:1 (upper row) and SB5:1 (lower row).

distribution of angles, one around $120°$ and another one at about $90°$. This maximum at $120°$ is established soon after crack formation has started and remains stable. The analysis at different times during crack formation indicates that in a later stage of crack formation, a second maximum is formed at $90°$. This corresponds to the observation that the branching of a developing crack most likely forms Y-junctions, while the coalescence of two individual cracks most likely forms T-junctions. The different types of junctions are related to the different formation processes, because

they correspond to the most efficient dissipation of energy.

6. Conclusions

We demonstrated that crack patterns in isotropic materials can be characterized by a few parameters, the $d+1$ Minkowski densities, where d is the dimension of the space considered. This greatly facilitates the comparison of cracking patterns in different materials,
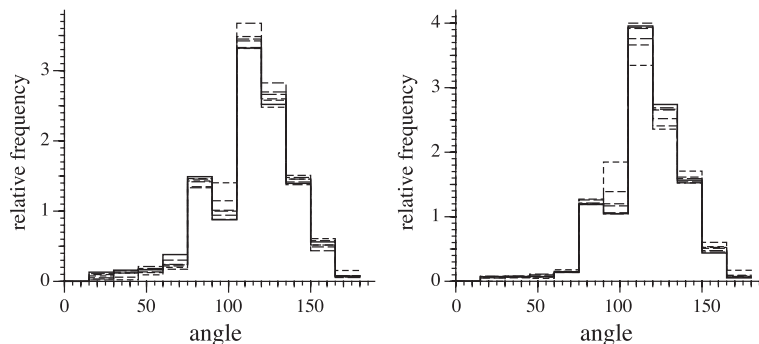

Fig. 8. Frequency distribution of angles of bifurcation after seven time intervals $\Delta t = t_{max}/7$ (dash lengths increase with time) for the crack patterns of SB1:1 (left) and SB5:1 (right).

as well as the description of the dynamics of a particular pattern. Obviously, such descriptions may be applied to real measurements, as it was demonstrated in this work, or to numerically simulated patterns that need to be compared with reality.

A powerful generalization of Minkowski densities are Minkowski functions, which calculate the densities as a function of the parameter(s) of some morphological transformation. We demonstrated this by considering erosions of the original soil cracks and aggregates, which represent "distance maps" from the crack pattern. In cracking soils, such maps have obvious significance for the dynamics of water, for the transport of solutes, and for the biological activity. We expect that their parameterization by a few numbers will greatly facilitate the formulation of corresponding effective models.

While Minkowski densities and functions go a long way towards a comprehensive characterization of crack patterns, they are not complete with respect to physical material properties, and more specific measures may be introduced for illuminating particular aspects. We demonstrated this with the distribution of bifurcation angles, and found that they peaked around two values, $90°$ and $120°$, corresponding to the optimal angles for a crack to join a preexisting one and for the bifurcation of an evolving crack, respectively.

Soil structure is not stationary, which is especially true for the nonlinear dynamics of crack formation. A geometric description of soil structure is typically related to the situation at a given time. This is a fundamental difficulty for any attempt to predict physical properties and processes based on quantitative morphology. Obviously, M_k and $M_k(r)$ can be employed to measure the dynamics of physical or simulated crack networks, and in particular to detect possibly critical transitions between different regimes. This approach is followed by a companion paper (Vogel et al., 2004), where a model of the nonlinear dynamics of shrinking cracks is developed.

Acknowledgments

References

Hadwiger, H., 1957. Vorlesung über Inhalt, Oberfläche und Isoperimetrie. Springer-Verlag, Berlin.

Hallaire, V., 1989. A 3-dimensional description of cracks networks in clayey soils, using image analysis and a structural model. Acta Stereol. 8/2, 301–306.

Kim, D.J., Jaramillo, R.A., Vauclin, M., Feyen, J., Choi, C.I., 1999. Modeling of soil deformation and water flow in a swelling soil. Geoderma 92, 217–238.

Mecke, K.R., 2000. Additivity, convexity, and beyond: applications of Minkowski functionals in statistical physics. Lect. Notes Phys. 554, 111–184.

C.J., Moran, 1994. Image processing and soil micromorphology, in Soil Micromorphology: Studies in Management and Genesis. In: Ringrose-Voase, A., Humphreys, G. (Eds.), Proceedings of the IX International Working Meeting on Soil Micromorphology, Townsville, Australia, July 1992. Elsevier, Amsterdam, pp. 459–482.

O'Callaghan, J.F., Loveday, J., 1973. Quantitative measurements of soil cracking patterns. Pattern Recogn. 5, 83–98.

Ohser, J., Mücklich, F., 2000. Statistical Analysis of Microstructures in Materials Science. J. Wiley and Sons, New York.

Preston, S., Griffiths, B.S., Young, I.M., 1997. An investigation into sources of soil crack heterogeneity using fractal geometry. Eur. J. Soil Sci. 48, 31–37.

Ringrose-Voase, A.J., Bullock, P., 1984. The automatic recognition and measurement of soil pore types by image analysis and computer programs. J. Soil Sci. 35, 673–684.

Samouëlian, A., Cousin, I., Richard, G., Tabbagh, A., Bruand, A., 2003. Electrical resistivity imaging for detecting soil cracking at the centimetric scale. Soil Sci. Soc. Am. J. 67, 1319–1326.

Scott, G.J., Webster, R., Nortcliff, S., 1986. An analysis of crack pattern in clay soil: its density and orientation. J. Soil Sci. 37, 653–668.

Serra, J., 1982. Image Analysis and Mathematical Morphology. Academic Press, London.

Tuller, M., Or, D., 2003. Hydraulic functions for swelling soils: pore scale considerations. J. Hydrol. 272, 50–71.

Velde, B., 1999. Structure of surface cracks in soil and muds. Geoderma 93, 101–124.

Vogel, H.J., Weller, U., Babel, U., 1993. Estimating orientation and width of channels and cracks at soil polished-blocks—a stereological approach. Geoderma 56, 301–316.

Vogel, H.J., Cousin, I., Roth, K., 2002. Quantification of pore structure and gas diffusion as a function of scale. Eur. J. Soil Sci. 53, 465–473.

Vogel, H.-J., Hoffmann, H., Leopold, A., Roth, K., 2004. Studies of crack dynamics in clay soil. II: a physically-based model for crack formation. Geoderma 125, 203–213 (this issue).